

Jamming is a first-order transition with quenched disorder in amorphous materials sheared by cyclic quasistatic deformations

Yue Deng,^{1,2} Deng Pan,¹ and Yuliang Jin^{1,2,3,*}

¹*CAS Key Laboratory of Theoretical Physics, Institute of Theoretical Physics, Chinese Academy of Sciences, Beijing 100190, China*

²*School of Physical Sciences, University of Chinese Academy of Sciences, Beijing 100049, China*

³*Center for Theoretical Interdisciplinary Sciences, Wenzhou Institute, University of Chinese Academy of Sciences, Wenzhou, Zhejiang 325001, China*

Jamming is an athermal transition between flowing and rigid states in amorphous systems such as granular matter, colloidal suspensions, complex fluids and cells. The jamming transition seems to display mixed aspects of a first-order transition, evidenced by a discontinuity in the coordination number, and a second-order transition, indicated by power-law scalings and diverging lengths. Here we demonstrate that jamming is a first-order transition with quenched disorder in cyclically sheared systems with quasistatic deformations. Particle models are simulated in two and three dimensions, which undergo reversible-irreversible transitions under cyclic shear. The ensemble of configurations, with partially crystallized and fragile states excluded, is generated in the irreversible phase, where the system is stationary and particles are diffusive. Detailed scaling analyses are performed on the distribution of coordination numbers. The fluctuation of the jamming density in finite-sized systems has important consequences on the finite-size effects of various quantities, resulting in a square relationship between disconnected and connected susceptibilities, a key signature of first-order transitions with quenched disorder. This study puts the jamming transition into the category of a broad class of transitions in disordered systems, including the first-order transition in the random-field Ising model, brittle yielding of amorphous materials, and melting of ultra-stable glasses.

Introduction.

Jamming in athermal particles is a paradigm of transitions between fluids and amorphous solids [1–5], with a deep connection to the glass transition in thermal systems [6–8]. Recent studies have revealed extremely rich features in the jamming phenomenon, but the nature of the jamming transition remains inconclusive.

(i) *Mechanical marginality, related diverging length scales and power-law scalings.* At the jamming transition density (volume fraction) φ_J , the isostatic condition needs to be satisfied for the coordination number Z (average number of contacts per particle): $Z = Z_{\text{iso}} = 2d$ in frictionless, infinite systems, where d is the dimensionality [9, 10]. Isostaticity implies that at φ_J the system is marginally stable, inspiring the search for diverging length scales. According to the “cutting argument”, the isostaticity gives rise to a diverging *isostatic length* scale at jamming, $l^* \sim \Delta Z^{-1} \sim (\varphi - \varphi_J)^{-1/2}$, below which mechanical stability of the bulk system is affected by the cutting boundaries [11–13], where $\Delta Z = Z - Z_{\text{iso}}$ is the excess coordination number. The effective medium theory gives a *scattering length* scale diverging at φ_J , $l_c \sim \Delta Z^{-1/2} \sim (\varphi - \varphi_J)^{-1/4}$, below which continuum elasticity breaks down [14–16]. Other related diverging length scales include the transverse wavelength, $\xi_T \sim (\varphi - \varphi_J)^{-\nu_T}$ with $\nu_T \approx 0.24$ [13], and the longitudinal wavelength, $\xi_L \sim (\varphi - \varphi_J)^{-\nu_L}$ with $\nu_L \approx 0.48$ [13].

At jamming, the marginal stability analysis provides relationships between the exponents θ appearing in the power-law distribution of weak inter-particle forces

$P(f) \sim f^\theta$ and α in the distribution of small inter-particle gaps $P(h) \sim h^{-\alpha}$: $\theta = 1/\alpha - 2$ for extensive modes [17] and $\theta = 1 - 2\alpha$ for localized buckling modes [18, 19]. Above jamming, the marginal boundary between unstable and stable phases is defined by a scaling relation, $\Delta Z \sim (\varphi - \varphi_J)^{1/2}$ [11, 20]. Other scalings have been established for over-jammed systems near φ_J [1–3, 5, 21, 22]. For example, a relationship between the shear modulus G and ΔZ can be derived by microscopic elastic theories, $G \sim \Delta Z \sim (\varphi - \varphi_J)^{1/2}$ [11, 23, 24].

(ii) *Hyperuniformity and associated diverging length scales.* Recent studies reveal the spatial distribution of the single-particle contact number, Z_i , is hyperuniform at jamming, implying a diverging *hyperuniform correlation length*, $\xi_H \sim \Delta Z^{-\nu}$ [25, 26]. The value of exponent ν appears to depend on the way to extract the correlation length and dimensionality [25].

(iii) *Gardner glass phase, landscape marginality and associated criticality.* The marginality at jamming has been established by an independent approach within the framework of replica symmetry breaking [8, 27–32]. Unjammed hard sphere glasses undergo a *Gardner transition* where the free energy landscape becomes fractal and marginal, and the caging susceptibility diverges [29]. The entire Gardner phase, including the jamming limit, is critical. In other words, the *caging correlation length* $\xi_G \sim (\varphi_J - \varphi)^0$ remains infinite near jamming. The mean-field replica theory predicts the values of exponents in the weak force and small gap distributions, $\alpha = 0.41269$ and $\theta = 0.42311$, coinciding with the relationship $\theta = 1/\alpha - 2$ given by the mechanical marginal stability analysis [27, 33, 34]. The theory provides an additional scaling relationship between the cage size Δ and

* yuliangjin@mail.itp.ac.cn

the entropic pressure p , $\Delta \sim p^{-\kappa}$ with $\kappa = 1.41574$. The exponents appear to be independent of the dimensionality d for $d \geq d_u$ [27, 33], where $d_u = 2$ is the conjectured upper critical dimension [35].

(iv) *Criticality in shear rheology.* The criticality of the jamming transition is suggested by scaling analysis of the rheological data obtained in finite-rate shear simulations of flowing states near φ_J [36–38]. Combing the power-law divergence of the viscosity, $\eta = (\varphi_J - \varphi)^{-\beta}$ and the vanishing of yield stress, $\sigma_Y \sim (\varphi - \varphi_J)^\Delta$, a critical scaling function is proposed. A diverging *rheological correlation length* can be extracted from velocity correlations [36] or non-affine displacements [39], $\xi_R \sim (\varphi_J - \varphi)^{-\nu}$, with $\nu = 0.6 - 1.1$ [36, 37, 39, 40]. The criticality seems to be at odds with the hyperuniformity discussed in (ii) – in the thermodynamical limit, the fluctuations diverge in the former and vanish in the latter.

(v) *Discontinuity in the coordination number.* The coordination number Z , which is considered as an order parameter of the jamming transition, jumps discontinuously from $Z = 0$ below jamming, to $Z \geq Z_{\text{iso}}$ above, in quasi-static compression or decompression [1, 2]. Apparently, as the signature of a first-order transition, this discontinuity is inconsistent with the viewpoints of a continuous transition described above.

It is clear that various diverging length scales have been suggested throughout the literature. However, none of the lengths in (i-iv) can explain the finite-size scaling behavior of the jamming fraction $F_J(\varphi, N)$ [2, 41–43]: the data can be reasonably collapsed by a master curve, $F_J(\varphi, N) = \mathcal{F}[(\varphi - \varphi_J)N^{1/2}]$, valid for both compression and shear jamming in two (2D) and three (3D) dimensions. In this study, we show that this scaling can be fully explained by a first-order transition scenario of the jamming transition with quenched disorder. The form $(\varphi - \varphi_J)N^{1/2}$ originates from the disorder-induced fluctuation of the jamming density itself in finite-sized systems of N particles, which follows the standard central limit theorem. Thus this finite-size scaling is independent of isostaticity, marginality, criticality and hyperuniformity.

Three important differences between previous approaches (i-v) and ours shall be denoted. First, in (i-iii), the jamming limit is approached from one side only, i.e., the over-jammed side ($\varphi > \varphi_J$) in (i) and (ii), and the unjammed side ($\varphi < \varphi_J$) in (iii). Here we consider a well-defined ensemble including both over-jammed and unjammed states, whose ratio is essential in the scaling analysis. Note that once an ensemble average is taken, the (v) discontinuity in Z turns into a smooth function, and thus a finite-size analysis becomes essential to see the asymptotic behavior in the thermodynamic limit.

Second, in conventional compression quenching protocols, the generated ensemble depends on the initial conditions [43–45] and the basins of attraction [41, 46, 47]. Here we instead consider an ensemble prepared by cyclic shear, where the states are sampled by well-controlled dynamics similar to that in thermal systems. Recently, the response of amorphous assemblies of particles to cyclic

shear has attracted great interest, due to the presence of a nonequilibrium phase transition, called the reversible-irreversible (RI) transition [48–52]. Interestingly, the jamming transition lies in the irreversible regime where particle trajectories are asymptotically diffusive [51, 52]. In this study, we restrict our ensemble within the irreversible phase.

Third, in our ensemble, we carefully exclude partially crystallized and fragile states with $Z < Z_{\text{iso}}$ that are sensitive to mechanical perturbations or protocol parameters, and regard them as unjammed states with $Z = 0$. If such states are included, the discontinuity in Z diminishes and the jamming transition looks continuous, similar to the results reported in Ref. [39] obtained by uniform shear. Thus we expect the impactibility between the criticality viewpoint in (iv) and our first-order picture originating from finite-rate effects. For finite-time scales, the existence of transient states with $Z < Z_{\text{iso}}$ can lead to a continuous jamming transition [36, 37, 39]. However, our results suggest that, after a sufficiently long time, any configurations with $Z < Z_{\text{iso}}$ would eventually relax to unjammed states with zero energy and inter-particle contacts.

An ensemble generated by cyclic athermal quasi-static shear.

We apply cyclic athermal quasistatic shear (CAQS) to standard models of soft, frictionless particles in 2D and 3D (see *Models* and *Shear protocol* in Methods). We present 2D data in the main text and 3D data in the Extended Data. For the 2D model, previous studies report a jamming density (J-point density) $\varphi_J \approx 0.842 - 0.843$ [40, 53]. The phase diagram of RI transitions near φ_J is plotted in Fig. 1a. The RI transition is characterized by the one-cycle displacement averaged over particles [51],

$$\delta r(t) = \frac{1}{N} \sum_{i=1}^N |\mathbf{r}_i(t+1) - \mathbf{r}_i(t)|, \quad (1)$$

and the mean-squared displacement (MSD),

$$\langle \Delta r^2(t) \rangle = \frac{1}{N} \left\langle \sum_{i=1}^N |\mathbf{r}_i(t) - \mathbf{r}_i(0)|^2 \right\rangle, \quad (2)$$

where t is the number of cycles playing a similar role as the time in thermal systems, $\mathbf{r}_i(t)$ the position of particle i at time t and zero strain $\gamma = 0$, and $\langle x \rangle$ the average over N_s samples.

The RI dynamics near φ_J are systematically studied in Ref. [51], according to which $\delta r(t)$ displays two-step relaxation behavior typically appearing in glassy systems. For $\tau_R < t < \tau_L$, $\delta r(t)$ develops a plateau at δr_s . In the interested *irreversible phase*, $\delta r_s > 0$, $\tau_R \sim 0$ and $\tau_L > t_{\text{max}}$ with t_{max} the maximum simulation time, suggesting that the system reaches a stationary state (see Fig. 1b). In addition, the MSD in the irreversible phase shows typical diffusive behavior $\langle \Delta r^2(t) \rangle \sim t$ (see

Fig. 1c). In contrast, in the *reversible phase*, $\delta r_s = 0$, which means that the system is “absorbed” into an invariant state. In practice, one defines $\delta r_\infty = \delta r(t_{\max})$ and distinguish between the reversible and irreversible phases by comparing the value of δr_∞ to a threshold δr_{th} . In this study, we set $t_{\max} = 4000$ and $\delta r_{\text{th}} = 0.1$, giving the boundary between irreversible (yellow) and reversible (blue) regions in Fig. 1a.

The above results imply that the configurational space is effectively explored by the dynamical trajectory of the system in the irreversible phase, encouraging us to consider a statistical ensemble generated by shear dynamics. In the main text below, we fix $\gamma_{\max} = 0.7$, and vary φ systematically in the window of $[0.833, 0.849]$. At each φ , in total $t_{\max} \times N_s$ independent configurations are collected to construct the ensemble. In the Extended Data, we present additional results obtained for $\gamma_{\max} = 1$. All configurations are typically isotropic since they are collected at $\gamma = 0$.

Figure 1d shows the time evolution of the coordination number $Z(t)$ in the irreversible phase, obtained from a typical simulation near φ_J . Rattlers (particles with fewer than $d + 1$ contacts) are removed in the computation of Z . At first glance, one sees the coexistence of jammed ($Z \approx 2d = 4$) and unjammed states ($Z = 0$), similar to the coexistence of two ferromagnetic states (positive m and negative m) in the time evolution of the magnetization $m(t)$ in an Ising model near a first-order phase transition [54]. However, a more careful examination reveals four distinct states, which we discuss below.

Four states: unjammed, jammed, partially crystallized and fragile.

In Fig. 2a, we plot the probability distribution $p(Z)$ of the states in the considered ensemble, at a fixed $\varphi = 0.841$ in the irreversible phase. The following four states, represented by peaks in $p(Z)$, can be identified (see Figs. 2e-h).

(i) *Unjammed states.* The left-most peak is a delta-function $p_U(Z) \sim \delta(Z)$, corresponding to unjammed states. All unjammed states have strictly zero contacts, $Z = 0$, once rattlers are removed.

(ii) *Jammed states.* The right-most peak $p_J(Z)$ at $Z \geq 4$ corresponds to jammed states. Their average coordination numbers satisfy minimally the isostatic condition, $Z \geq 2d = 4$.

(iii) *Partially crystallized states.* The delta-peak at $p_C(Z) \sim \delta(Z - 24/7)$ represents the states with a single unit cell of the hexagonal crystal (see Fig. 2e). Here $24/7 \approx 3.4286$ is the average number of contacts of the seven particles forming the unit cell. Occasionally, states with two or three unit crystal cells can be also found but they are rare.

(iv) *Fragile states.* We define the states in the broad peak $3 < Z < 4$, excluding the crystalline peak $p_C(Z)$ as the fragile states.

The fractions, F_U , F_J , F_C and F_F , of the above four states (i-iv), are obtained by integrating corresponding

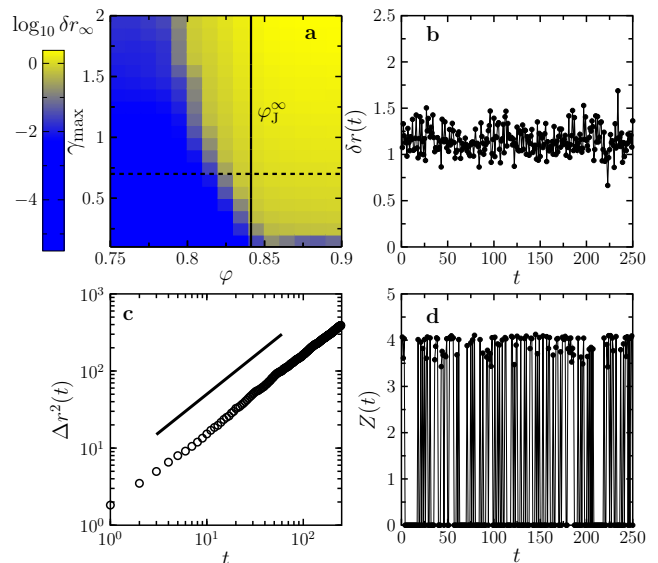


FIG. 1. **Cyclic athermal quasi-static shear simulations.** (a) Reversible ($\delta r_\infty < 0.1$, blue region) and irreversible ($\delta r_\infty > 0.1$, yellow region) phases ($N = 1000$). The solid line represents $\varphi_J^\infty = 0.8432$, and the dashed line represents $\gamma_{\max} = 0.7$ used to generate the ensemble in the main text. (b) One-cycle displacement $\delta r(t)$ and (d) average coordination number $Z(t)$ for a typical sample. (c) The MSD data show diffusive behavior $\langle \Delta r^2(t) \rangle \sim t$ (line). Data in (b-c) are obtained at a fixed $\varphi = 0.841$.

peaks in $p(Z)$. In Fig. 2b, the fractions are plotted as functions of φ , showing that $F_J(\varphi)$ increases from zero to one across φ_J . This behavior is quantitatively similar to $F_J(\varphi)$ obtained in previous rapid quench simulations, where finite-size analyses have been carried out to precisely determine the asymptotic jamming transition density φ_J^∞ in the thermodynamic limit $N \rightarrow \infty$ [2, 40]. We will perform such finite-size analyses later, after discussing the nature of fragile states.

In Fig. 2c, we report various fractions as functions of t at $\varphi = 0.841$. The fractions are independent of t , confirming that the system is stationary. We further divide $F_C(t)$ into two parts, $F_C(t) = F_C^1(t) + F_C^>(t)$, where $F_C^1(t)$ and $F_C^>(t)$ are respectively the fractions of partially crystallized states with one and more than one crystal unit cells. Both $F_C^1(t)$ and $F_C^>(t)$ are independent of t , indicating that the growth of seed crystals is not observed. Because F_C is generally several orders of magnitude lower than the fractions of other types, partially crystallized states will be ignored in the following analyses.

In Fig. 2d, we plot the maximum coordination numbers, Z_J^* and Z_U^* , of jammed and fragile peaks. Around φ_J , there is a small gap $\delta Z_{\text{gap}} \approx 0.2$ between Z_J^* (upper branch) and Z_U^* (lower branch). The results are very similar to those obtained by quasistatic uniform shear in Ref. [39] (see Fig. 4 therein). In Ref. [39], it is suggested that δZ_{gap} vanishes in the thermodynamic limit, and thus the jamming transition is continuous. However, as

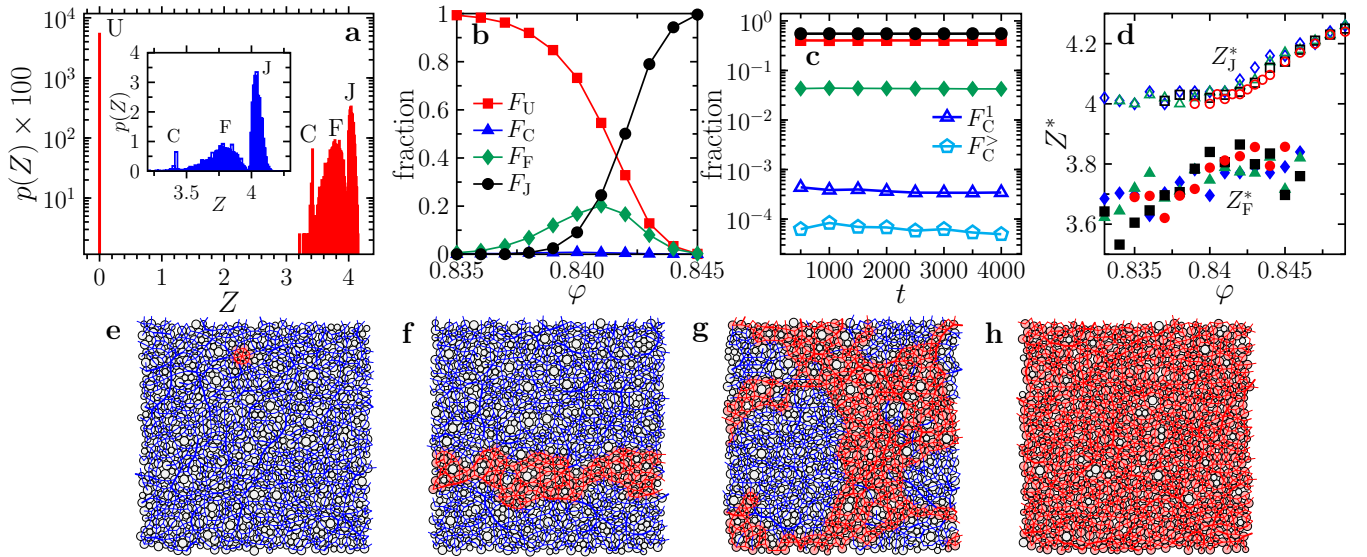


FIG. 2. **Four states.** (a) Semi-log plot of the probability distribution $p(Z)$. The four peaks of unjammed (U), partially crystallized (C), fragile (F) and jammed (J) states, are indicated. The inset shows a linear plot of $p(Z)$ without the unjammed peak. Fractions are plotted as a function of φ in (b), and of t in (c). In (c), each data point is obtained for a small window $[t - \delta t, t + \delta t]$ with $\delta t = 250$. (d) Peak coordination numbers Z_J^* of jammed states (upper branch, open symbols) and Z_F^* of fragile states (lower branch, filled symbols) as functions of φ , for $N = 256$ (diamonds), 512 (triangles), 1000 (squares), and 2000 (circles). In (e-h), we show typical configurations of (e) partially crystallized, (f) fragile percolating in one direction, (g) fragile percolating in both directions, and (h) jammed states. Contact forces are represented by bonds, whose width is proportional to the magnitude of force. The red and blue disks are non-rattler and rattler particles respectively. We set $\varphi = 0.841$ for (a) and (c), $N = 256$ for (b) and (c), and $N = 1000$ for (e-h).

we show below, the fragile states are generated due to incomplete energy minimization and are mechanically unstable. Once such fragile states are excluded, the lower branch only contains unjammed states with $Z_U^* = 0$, which is separated by a large gap $\delta Z_{\text{gap}} \approx 4$ from the upper branch $Z_J^* \geq 4$.

Instability of fragile states.

Previously, the fragile states were obtained by *uniform shear* at non-zero strains $\gamma > 0$ below φ_J in experiments [55] and simulations [56]. It was proposed that fragile and jammed states differ in the percolation of the strong force network: in fragile states the percolation occurs anisotropically in one direction only, while in jammed states it occurs isotropically in both directions. In this study, all states are collected during *cyclic shear* at $\gamma = 0$, without systematically introducing anisotropy. Indeed, the fragile states with $3 < Z < 4$ can have percolated force networks of non-rattlers in one or two directions (see Fig. 2f and g). Thus in our case, anisotropy cannot effectively distinguish fragile from jammed states.

We demonstrate that the essential difference between fragile and jammed states is their mechanical stability. In fragile states, the potential energy per particle is negligibly low (see *Stopping criterion for energy minimization* in Methods), $\bar{e}_i < e_{\text{th}} = 10^{-20}$ (see Fig. 3a), but the fraction of non-rattler particles is non-zero. These non-rattlers experience forces, which can form a transient,

percolated network. Such networks are highly heterogeneous (see Fig. 2f and g), compared to those in jammed states (see Fig. 2h). More importantly, the force networks in fragile states are unstable, revealed by the non-zero net force per particle, $\bar{f}_i > f_{\text{th}} = 10^{-14}$ (see Fig. 3b). Thus fragile states are not strictly equilibrated; they turn into unjammed states by sufficiently long relaxation (accurate energy minimization) or mechanical perturbations.

To demonstrate the instability of fragile states, two tests are carried out. First, we perform a compression-decompression perturbation, $\varphi \rightarrow \varphi + \delta\varphi \rightarrow \varphi$, where $\delta\varphi = 10^{-8}$, and the energy is minimized after each step. All fragile states ($3 < Z < 4$) become unjammed ($Z = 0$) after this perturbation, while jammed states remain. In Fig. 3c, we plot the distribution $p'(Z)$ after the compression-decompression perturbation. Independently, without any perturbation we simply regard all fragile states ($3 < Z < 4$) as unjammed ($Z = 0$) and recalculate the distribution $\tilde{p}(Z)$. Figure 3c shows that the two distributions $p'(Z)$ and $\tilde{p}(Z)$ perfectly coincide.

In the second test, we repeat CAQS simulations by systematically varying the threshold f_{th} in the criterion of the energy minimization algorithm. The fraction F_F of fragile states grows and F_U of unjammed states decays with increasing f_{th} (Fig. 3d), suggesting that many unjammed states become fragile under a looser force-balance condition $\bar{f}_i < f_{\text{th}}$ with a larger f_{th} . In contrast, the constant F_J shows that the definition of jammed

states is insensitive to the algorithm parameter. Note that in granular experiments [55, 57], the friction may play the role of f_{th} , i.e., the net inter-particle force could be balanced by the frictional force between particles and the supporting plate. According to this assumption, the probability of observing fragile states in experiments would depend on the particle-plate friction that can be changed by replacing the materials. It provides a protocol to examine our scenario of fragile states in future experimental studies.

Because fragile states are unstable, from now on we count them as unjammed states. More specifically, we replace the original distribution $p(Z)$ with the modified distribution $\tilde{p}(Z)$. For simplicity, we omit the tilde and denote $\tilde{p}(Z)$ by $p(Z)$ below.

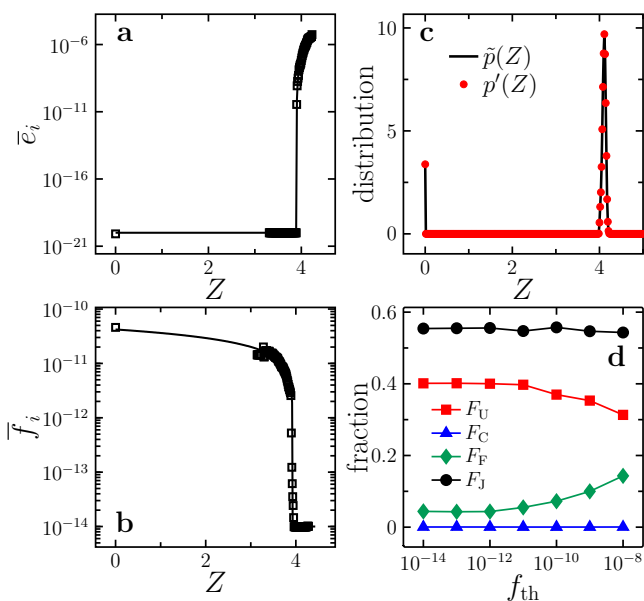


FIG. 3. **Stability tests.** Average single-particle (a) potential energy \bar{e}_i and (b) net force \bar{f}_i as functions of Z . Lines in (a) and (b) are guides to the eye. (c) Comparison between $p'(Z)$ obtained after the compression-decompression perturbation and $\tilde{p}(Z)$ with fragile states counted as unjammed states, for $N = 1000$ at $\varphi = 0.844$. (d) Fractions of four states as functions of f_{th} . Data are obtained for $N = 256$ systems, except for (c).

Scaling analysis of $p(Z)$ near the jamming transition.

The new distribution $p(Z)$ contains two peaks of unjammed and jammed states, whose fractions satisfy $F_U(\varphi) + F_J(\varphi) = 1$ at any φ . In Figs 4a and b, we plot $p(Z)$ for a few different φ and N , showing that $p(Z)$ is always double-peaked across the jamming transition, which is typical behavior of a first-order rather than a second-order transition.

To analyze the scaling behavior of $p(Z)$, we consider a general first-order form of first-order phase transi-

tions [54, 58],

$$p(Z) = (1 - F_J)\delta(Z) + F_J p_J [(Z - Z_J^*)N^\eta], \quad (3)$$

where $\delta(Z)$ and $p_J(Z)$ correspond to the unjammed and jammed peaks respectively. The asymptotic jamming density $\varphi_J^\infty = 0.8432$ for $N \rightarrow \infty$ is determined by the intersection of $F_J(\varphi)$ curves with different N (see Fig. 4c), close to the J-point density $\varphi_J \approx 0.842 - 0.843$ reported in previous studies [2, 40]. The difference between $\varphi_J^\infty = 0.8432$ by $\gamma_{\text{max}} = 0.7$ and $\varphi_J^\infty = 0.8435$ by $\gamma_{\text{max}} = 1$ (see Extended Data Fig. E1) is too small to conclude any systematic dependence on γ_{max} . In Ref. [52], an unjamming pocket is reported in the phase diagram for $\gamma_{\text{max}} < 0.17$, while for larger γ_{max} , φ_J is independent of γ_{max} , consistent with our observations. These results also suggest that the jamming density obtained by cyclic shear is the lowest jamming density on the J-line of all possible jammed states [6, 44, 59].

As shown in Fig. 2d, Z_J^* is independent of N near φ_J , and weakly depends on φ . In the following scaling analysis, Z_J^* is approximated by a constant value $Z_J^* \approx 4.1$ at $\varphi_J^\infty = 0.8432$. To keep the expressions concise, we ignore the corrections to the scaling functions from the φ -dependence of Z_J^* .

We assume the fraction of jammed states F_J having the following scaling form, $F_J(\varphi, N) = \mathcal{F}[(\varphi - \varphi_J^\infty)N^\lambda]$. The value of the exponent λ is important for understanding the nature of the transition. If the system were thermal, the fraction would be determined by the Boltzmann distribution, $F_J \sim \exp\left(\frac{N\delta f}{k_B T}\right)$, where δf is the single-particle free energy difference between two phases [54, 58]. Because the free energy is non-singular around a first-order phase transition, it can be expanded, giving $\delta f \sim (T - T_c)$ to the lowest order. Thus, if the jamming transition were a standard first-order phase transition, then $F_J(\varphi, N) = \mathcal{F}_J[(\varphi - \varphi_J^\infty)N]$, i.e., $\lambda = 1$ (note that φ in the granular system is analogous to the temperature T in thermal systems). However, our numerical data can not be collapsed using $\lambda = 1$; in contrast, they can be perfectly collapsed using $\lambda = 1/2$ (see Fig. 4d).

To understand the origin of $\lambda = 1/2$ scaling, recall that the athermal jamming transition is not driven by the free energy difference between the two phases. Below we explain the scaling by the scenario of a first-order transition with quenched disorder. For a finite N , due to the presence of disorder in the packing structure, the jamming density φ_J^N should fluctuate around the asymptotic value φ_J^∞ . Let us assume a simple Gaussian form of the distribution, $\rho(\varphi_J^N) \sim \exp\left[-\frac{(\delta\hat{\varphi}_J + u)^2}{2\sigma_\varphi^2}\right]$, where $\delta\hat{\varphi}_J = (\varphi_J^N - \varphi_J^\infty)N^{1/2}$ follows the standard central limit theorem. Note that $\rho(\varphi_J^N)$ has been explicitly measured in the compression protocol [2, 53]: the width of $\rho(\varphi_J^N)$ scales as $w \sim N^{-0.55}$ in both 2D and 3D, supporting our assumption. The above assumption also predicts, $\varphi_J^\infty - \varphi_J^N \sim N^{-1/2}$, independent of dimensionality. The

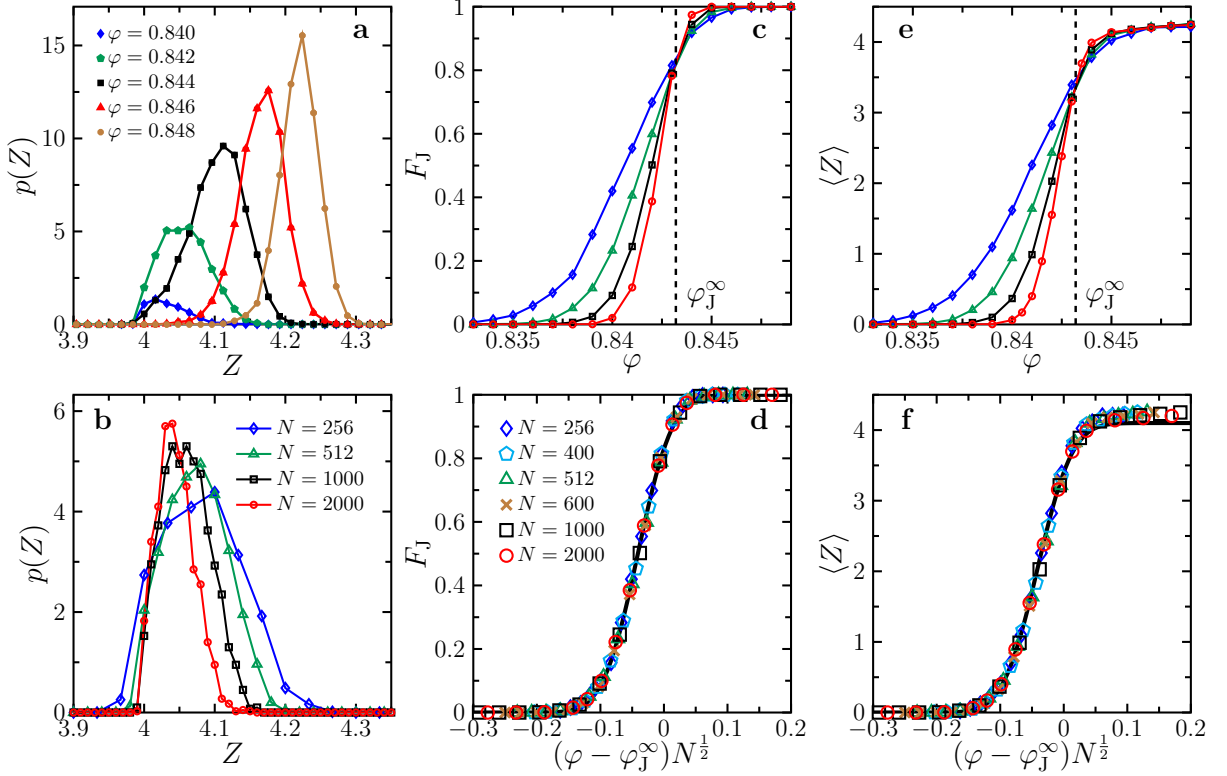


FIG. 4. **Distribution of the coordination number.** (a) Probability distribution $p(Z)$ at a few different φ for $N = 1000$. (b) $p(Z)$ at $\varphi = 0.843$ for a few different N . For better visualization, we do not show the unjammed delta-peak at $Z = 0$. (c) The fraction of jammed states F_J as a function of φ for a few different N . The intersection of curves gives $\varphi_J^\infty = 0.8432$. (d) The data points of F_J with different N collapse as a function of $(\varphi - \varphi_J^\infty)N^{1/2}$. The solid line represents fitting to Eq. (4), with two fitting parameters $u = 0.041$ and $\sigma_\varphi = 0.043$. The average coordination number $\langle Z \rangle$ is plotted as a function of φ in (e) and of $(\varphi - \varphi_J^\infty)N^{1/2}$ in (f). The solid line in (f) represents $\langle Z \rangle = F_J Z_J^*$ using $u = 0.041$, $\sigma_\varphi = 0.043$ and $Z_J^* = 4.1$. Symbols in (b-f) have the same meanings.

jammed states are defined by $\varphi > \varphi_J^N$, and thus

$$F_J(\varphi, N) = \int_0^\varphi \rho(\varphi_J^N) d\varphi_J^N \approx \frac{1}{2} + \frac{1}{2} \operatorname{erf} \left[\frac{\delta\hat{\varphi} + u}{\sqrt{2}\sigma_\varphi} \right], \quad (4)$$

where $\delta\hat{\varphi} = (\varphi - \varphi_J^\infty)N^{1/2}$. Equation (4) agrees well with the data in Fig. 4d.

Once the scaling behavior of $F_J(\varphi, N)$ is obtained, it is easy to derive scaling forms of susceptibilities. In the random field Ising model (RFIM) [60, 61], two susceptibilities have been introduced: a *connected susceptibility* χ_{con} associated to thermal fluctuations, and a *disconnected susceptibility* χ_{dis} associated to fluctuations caused by disorder. The two susceptibilities are related by $\chi_{\text{dis}} = \chi_{\text{con}}^2$ around the critical point and first-order transitions in RFIM. We similarly define two susceptibilities in the jamming transition. The disconnected susceptibility is defined as $\chi_{\text{dis}} \equiv N\sigma_Z^2 = N\langle (Z - \langle Z \rangle)^2 \rangle$, where σ_Z^2 is the variance of $p(Z)$ and $\langle \dots \rangle$ is the average over all states. From Eq. (3), we obtain,

$$\frac{\chi_{\text{dis}}(\varphi, N)}{N} \approx (Z_J^*)^2 [1 - F_J(\varphi, N)] F_J(\varphi, N), \quad (5)$$

where $F_J(\varphi, N)$ is given by Eq. (4). Equation (5) suggests a scaling form $\chi_{\text{dis}}(\varphi, N)/N = \chi_{\text{dis}} [(\varphi - \varphi_J^\infty)N^{1/2}]$, in agreement with the data in Fig. 5a.

The alternative connected susceptibility is defined as $\chi_{\text{con}} = d\langle Z \rangle / d\varphi$. From Eq. (3), one finds that $\langle Z \rangle \approx F_J Z_J^*$ and thus $\langle Z \rangle$ has the same scaling form as F_J , i.e., $\langle Z \rangle(\varphi, N) = \mathcal{Z} [(\varphi - \varphi_J^\infty)N^{1/2}]$, consistent with the data in Fig. 4e and f. Using $\chi_{\text{con}} = Z_J^* \frac{dF_J}{d\varphi}$ and Eq. (4), we derive,

$$\frac{\chi_{\text{con}}(\varphi, N)}{N^{1/2}} \approx \frac{Z_J^*}{\sigma_\varphi \sqrt{2\pi}} \exp \left[- \left(\frac{\delta\hat{\varphi} + u}{\sqrt{2}\sigma_\varphi} \right)^2 \right], \quad (6)$$

which is verified by the simulation data in Fig. 5b.

Now we can look at the relationship between χ_{dis} and χ_{con} . Expanding Eqs. (5) and (6) around the maxima, where $x \equiv \frac{\delta\hat{\varphi} + u}{\sqrt{2}\sigma_\varphi} = 0$, we obtain, up to the quadratic order,

$$\frac{\chi_{\text{dis}}}{\chi_{\text{con}}^2} \approx \frac{\pi\sigma_\varphi^2}{2} \left[1 + \left(2 - \frac{4}{\pi} \right) \left(\frac{\delta\hat{\varphi} + u}{\sqrt{2}\sigma_\varphi} \right)^2 \right]. \quad (7)$$

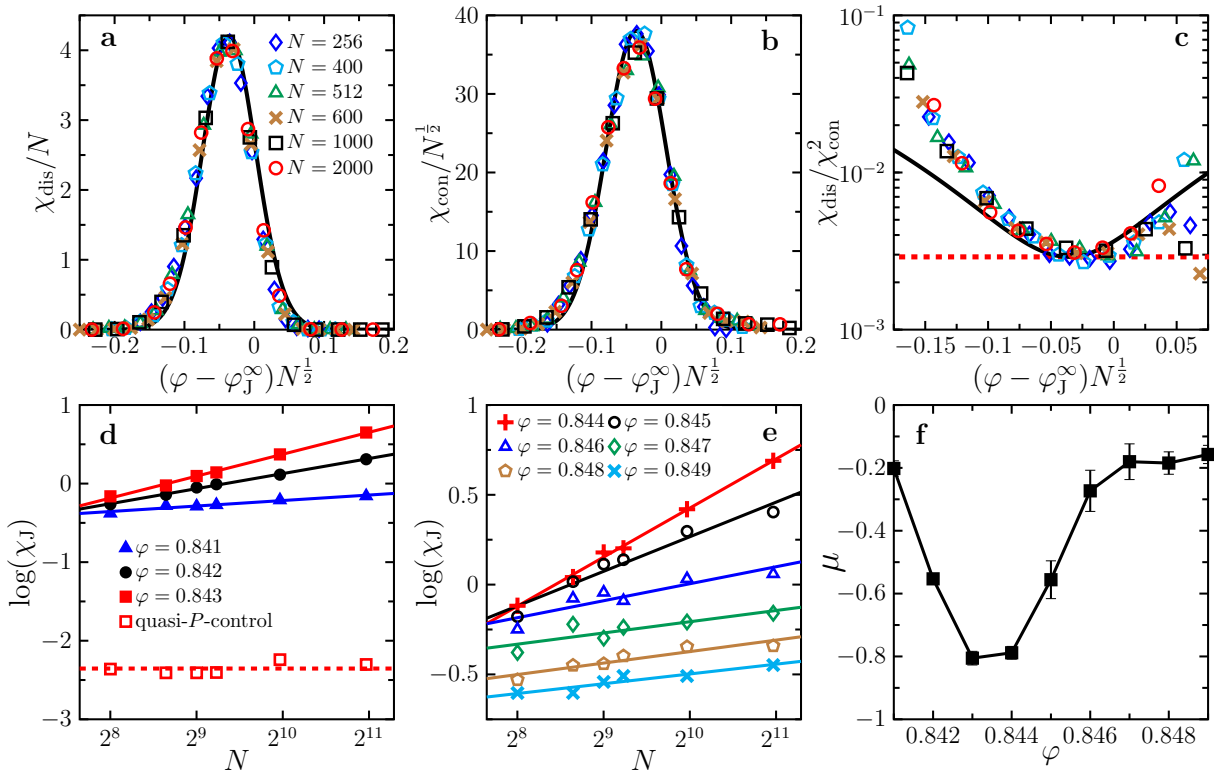


FIG. 5. **Susceptibilities.** We plot (a) the disconnected susceptibility χ_{dis} rescaled by N , (b) the connected susceptibility χ_{con} rescaled by $N^{3/2}$, and (c) the ratio between χ_{dis} and χ_{con} , as functions of $(\varphi - \varphi_J^\infty)N^{1/2}$. The solid black lines in (a-c) are Eqs. (5), (6) and (7) respectively. The dashed red line in (c) is the constant term in Eq. (7), i.e., $\chi_{\text{dis}}^2/\chi_{\text{con}}^2 = \pi\sigma_\varphi^2/2$. To draw these lines, we use $u = 0.036$ and $\sigma_\varphi = 0.043$ obtained from the fitting in Fig. 4d, and $Z_J^* = 4.1$ determined at $\varphi_J^\infty = 0.8432$ in Fig. 2d. No fitting is performed here. Symbols in (a-c) have the same meanings as indicated in the legend of (a). In (d) and (e), the susceptibilities of jammed states χ_J are plotted as functions of N for a few different φ , and are fitted to Eq. (8). The open squares in (d) are χ_J data obtained in a small pressure window $0.0009 < P < 0.0011$, corresponding to $\varphi \approx 0.843$. The fitting parameter μ is plotted in (f) as a function of φ , where the error bar represents the fitting error.

To the lowest order, Eq. (7) gives a scaling, $\chi_{\text{dis}} \sim \chi_{\text{con}}^2$, which is a key signature of the presence of quenched disorder. This square relationship appears generally at first-order transitions in disordered systems, such as the first-order phase transition in the RFIM [61], the brittle yielding of amorphous solids [62] and the melting of ultrastable hard-sphere glasses [63]. Comparing to the simulation data, Eq. (7) works well around the extreme point (see Fig. 5c).

It seems that the non-Gaussian effect in the distribution $\rho(\varphi_J^N)$, which is neglected in the present analysis, is amplified in the data of $\chi_{\text{dis}}/\chi_{\text{con}}^2$, resulting in slight asymmetry. Extended Data Figs. E1-E4 show that the scaling functions Eqs. (4)-(7) work in 3D, and for a different max strain $\gamma_{\text{max}} = 1$ in 2D.

Finally let us discuss the finite-size effects of the jammed peak $p_J(Z)$ in Eq. (3). For standard first-order phase transitions, $\eta = 1/2$ [54, 58]. Thus in that scenario the susceptibility of the jamming peak would scale as, $\chi_J \equiv N\sigma_J^2 = N\langle(Z - Z_J^*)^2\rangle_J \sim N^0$, where σ_J^2 is the variance of $p_J(Z)$ and $\langle \dots \rangle_J$ represents the average restricted to the jammed states only. However, our χ_J data disagree

with this scaling (see Figs. 5d-f). At different φ , χ_J can be fitted to a power-law form,

$$\chi_J \sim N^{-\mu/d}, \quad (8)$$

where $\mu = d(2\eta - 1)$ is a fitting parameter. At large or small φ away from φ_J^∞ (see Fig. 5f), the exponent is close to zero ($\mu \approx -0.2$), suggesting that the local coordination numbers Z_i are uniformly distributed. The deviation from the uncorrelated behavior ($\mu = 0$) is significant around φ_J^∞ , where $\mu \approx -0.8$ reaches the minimum.

The result of μ shall be interpreted with care. In general, (i) $\mu = 0$ corresponds to uniformity of Z_i , (ii) $\mu > 0$ to hyperuniformity with a vanishing χ_J in the thermodynamic limit, and (iii) $\mu < 0$ to hyperfluctuations with a diverging χ_J in the thermodynamic limit that typically appears at the critical point in a second-order phase transition. However, the negative μ in Fig. 5f is not due to the criticality of the jamming transition. Here it is essential to consider the volume fluctuations. The negative μ is obtained from a φ -controlled setup in our CAQS simulations. If we instead select configurations around a constant pressure P , then the fluctuations

become significantly smaller, and $\mu \approx 0$ (Fig. 5d). This observation is consistent with a previous study [64], suggesting that the large fluctuation of Z near φ_J^∞ in the φ -controlled protocol might be originated from the fluctuation of φ_J^N . In fact, careful measurement gives $\mu \simeq 1$ in a P -controlled protocol at jamming, confirming hyperuniformity [25, 26]. We emphasize that the finite-size effects of the jammed peak $p_J(Z)$ contribute negligibly to the scaling of $F(\varphi, N)$, $\chi_{\text{dis}}(\varphi, N)$ and $\chi_{\text{con}}(\varphi, N)$. In other words, the first-order nature of the jamming transition is independent of how Z_i is spatially distributed in jammed packings.

Conclusion.

In this study, we understand the nature of jamming transition through an ensemble approach analogous to the statistical mechanics in equilibrium systems [22, 65]. Within such a framework, the order of the jamming transition is independent of the complex properties of jammed packings, including isostaticity, marginality and hyperuniformity (see (i-iii) in Introduction). As a first-order jamming transition, the finite-size scaling exponents measured in this study are naturally universal in 2D and 3D, without the need to introduce the upper critical dimension $d_u = 2$ [66], a concept relevant to continuous transitions only. It is of particular interest to reconcile the first-order transition established here under quasi-static shearing and the second-order transition observed in previous finite-rate rheology (see (iv) in Introduction). The jamming transition appears to be a rare example with the simultaneous existence of first-order and second-order transitions between liquid and solid states. Conventionally, the two kinds of transitions only coexist in gas-liquid systems, but not in liquid-crystalline solid systems.

Methods.

Models. We study models of frictionless, bidisperse particles in two and three dimensions. The number ratio between large and small particles is 1:1, and the diameter ratio is 1.4:1. The potential energy between two particles is:

$$U(r_{ij}) = \frac{\epsilon}{2} \left(1 - \frac{r_{ij}}{\sigma_{ij}}\right)^2 \Theta\left(1 - \frac{r_{ij}}{\sigma_{ij}}\right), \quad (9)$$

where $\epsilon = 1$ is the energy unit, r_{ij} the distance between

particles i and j , $\sigma_{ij} = \frac{\sigma_i + \sigma_j}{2}$ the mean diameter, and $\Theta(x)$ the Heaviside step function. We set unit particle mass, and the diameter of small particles as unit length.

Shear protocol. Particles are randomly distributed at an initial volume fraction $\varphi_0 = 0.02$. The system is then rapidly quench compressed to the target φ . The CAQS is performed under the Lees-Edwards boundary conditions, with a fixed φ . We use a strain step $\delta\gamma = 0.1$ to generate the phase diagram in Fig. 1a, and $\delta\gamma = 0.01$ for other results. At each step, particle positions are shifted according to $x_i \rightarrow x_i + \delta\gamma y_i$, and then the system's energy is minimized using the FIRE algorithm [67]. During a cycle, the strain is varied as $\gamma = 0 \rightarrow \gamma_{\text{max}} \rightarrow 0$. We set $\gamma_{\text{max}} = 0.7$ in the main text and $\gamma_{\text{max}} = 1$ in the Extended Data for the 2D model, and $\gamma_{\text{max}} = 0.5$ for the 3D model (Extended Data). The number of cycles is represented by t with unit oscillation period ($t = 1$). In 2D, the maximum number of cycles is $t_{\text{max}} = 250$ for $0.839 \leq \varphi \leq 0.849$ and $t_{\text{max}} = 4000$ for $0.833 \leq \varphi < 0.839$, while in 3D, $t_{\text{max}} = 144$ for 2000, and $t_{\text{max}} = 50$ for $N = 512$ and 1000. We generate $N_s = 4000 - 12000$ independent samples at each φ . At each φ , in total $t_{\text{max}} \times N_s$ configurations are collected to compute statistical quantities.

Stopping criterion for energy minimization. We terminate the energy minimization when the potential energy per particle $\bar{e}_i = \frac{1}{N} \sum_{i=1}^N e_i$ falls below a threshold e_{th} or the average single-particle net force $\bar{f}_i = \frac{1}{N} \sum_{i=1}^N f_i$ falls below f_{th} , whichever is satisfied earlier. We set $e_{\text{th}} = 10^{-20}$ and $f_{\text{th}} = 10^{-14}$ unless otherwise specified.

ACKNOWLEDGMENTS

We warmly thank Hajime Yoshino for inspiring discussions. We acknowledge financial support from NSFC (Grants 12161141007, 11935002, 11974361 and 12047503), from Chinese Academy of Sciences (Grants ZDBS-LY-7017 and KGFZD-145-22-13), and from Wenzhou Institute (Grant WIUCASQD2023009). In this work access was granted to the High-Performance Computing Cluster of Institute of Theoretical Physics - the Chinese Academy of Sciences.

-
- [1] Hernán A Makse, David L Johnson, and Lawrence M Schwartz, "Packing of compressible granular materials," Physical review letters **84**, 4160 (2000).
 [2] Corey S O'hern, Leonardo E Silbert, Andrea J Liu, and Sidney R Nagel, "Jamming at zero temperature and zero applied stress: The epitome of disorder," Physical Review E **68**, 011306 (2003).
 [3] Andrea J Liu and Sidney R Nagel, "The jamming transi-

- tion and the marginally jammed solid," Annu. Rev. Condens. Matter Phys. **1**, 347–369 (2010).
 [4] Martin van Hecke, "Jamming of soft particles: geometry, mechanics, scaling and isostaticity," Journal of Physics: Condensed Matter **22**, 033101 (2009).
 [5] Deng Pan, Yinqiao Wang, Hajime Yoshino, Jie Zhang, and Yuliang Jin, "A review on shear jamming," Physics Reports **1038**, 1–18 (2023), a review on shear jamming.

- [6] Giorgio Parisi and Francesco Zamponi, “Mean-field theory of hard sphere glasses and jamming,” *Reviews of Modern Physics* **82**, 789 (2010).
- [7] Patrick Charbonneau, Jorge Kurchan, Giorgio Parisi, Pierfrancesco Urbani, and Francesco Zamponi, “Glass and jamming transitions: From exact results to finite-dimensional descriptions,” *Annual Review of Condensed Matter Physics* **8**, 265–288 (2017).
- [8] Giorgio Parisi, Pierfrancesco Urbani, and Francesco Zamponi, *Theory of simple glasses: exact solutions in infinite dimensions* (Cambridge University Press, 2020).
- [9] J Clerk Maxwell, “I.—on reciprocal figures, frames, and diagrams of forces,” *Earth and Environmental Science Transactions of the Royal Society of Edinburgh* **26**, 1–40 (1870).
- [10] Shlomo Alexander, “Amorphous solids: their structure, lattice dynamics and elasticity,” *Physics reports* **296**, 65–236 (1998).
- [11] M Wyart, “On the rigidity of amorphous solids,” in *Annales de Physique*, Vol. 30 (EDP Sciences, 2005) pp. 1–96.
- [12] “Geometric origin of excess low-frequency vibrational modes in weakly connected amorphous solids,” *Europhysics Letters* **72**, 486 (2005).
- [13] Leonardo E Silbert, Andrea J Liu, and Sidney R Nagel, “Vibrations and diverging length scales near the unjamming transition,” *Physical review letters* **95**, 098301 (2005).
- [14] Matthieu Wyart, “Scaling of phononic transport with connectivity in amorphous solids,” *Europhysics Letters* **89**, 64001 (2010).
- [15] Eric DeGiuli, Adrien Laversanne-Finot, Gustavo Düring, Edan Lerner, and Matthieu Wyart, “Effects of coordination and pressure on sound attenuation, boson peak and elasticity in amorphous solids,” *Soft matter* **10**, 5628–5644 (2014).
- [16] Edan Lerner, Eric DeGiuli, Gustavo Düring, and Matthieu Wyart, “Breakdown of continuum elasticity in amorphous solids,” *Soft Matter* **10**, 5085–5092 (2014).
- [17] Matthieu Wyart, “Marginal stability constrains force and pair distributions at random close packing,” *Physical review letters* **109**, 125502 (2012).
- [18] Edan Lerner, Gustavo Düring, and Matthieu Wyart, “Low-energy non-linear excitations in sphere packings,” *Soft Matter* **9**, 8252–8263 (2013).
- [19] Eric DeGiuli, Edan Lerner, Carolina Brito, and Matthieu Wyart, “Force distribution affects vibrational properties in hard-sphere glasses,” *Proceedings of the National Academy of Sciences* **111**, 17054–17059 (2014).
- [20] Markus Müller and Matthieu Wyart, “Marginal stability in structural, spin, and electron glasses,” *Annu. Rev. Condens. Matter Phys.* **6**, 177–200 (2015).
- [21] Carl P Goodrich, Andrea J Liu, and James P Sethna, “Scaling ansatz for the jamming transition,” *Proceedings of the National Academy of Sciences* **113**, 9745–9750 (2016).
- [22] Adrian Baule, Flaviano Morone, Hans J Herrmann, and Hernán A Makse, “Edwards statistical mechanics for jammed granular matter,” *Reviews of modern physics* **90**, 015006 (2018).
- [23] Alessio Zaccone and Enzo Scossa-Romano, “Approximate analytical description of the nonaffine response of amorphous solids,” *Physical Review B* **83**, 184205 (2011).
- [24] Deng Pan, Fanlong Meng, and Yuliang Jin, “Shear hardening in frictionless amorphous solids near the jamming transition,” *PNAS nexus* **2**, pgad047 (2023).
- [25] Daniel Hexner, Andrea J Liu, and Sidney R Nagel, “Two diverging length scales in the structure of jammed packings,” *Physical review letters* **121**, 115501 (2018).
- [26] Daniel Hexner, Pierfrancesco Urbani, and Francesco Zamponi, “Can a large packing be assembled from smaller ones?” *Physical review letters* **123**, 068003 (2019).
- [27] Patrick Charbonneau, Jorge Kurchan, Giorgio Parisi, Pierfrancesco Urbani, and Francesco Zamponi, “Fractal free energy landscapes in structural glasses,” *Nature communications* **5**, 3725 (2014).
- [28] Patrick Charbonneau, Yuliang Jin, Giorgio Parisi, Corrado Rainone, Beatriz Seoane, and Francesco Zamponi, “Numerical detection of the gardner transition in a mean-field glass former,” *Physical Review E* **92**, 012316 (2015).
- [29] Ludovic Berthier, Patrick Charbonneau, Yuliang Jin, Giorgio Parisi, Beatriz Seoane, and Francesco Zamponi, “Growing timescales and lengthscales characterizing vibrations of amorphous solids,” *Proceedings of the National Academy of Sciences* **113**, 8397–8401 (2016).
- [30] Ludovic Berthier, Giulio Biroli, Patrick Charbonneau, Eric I Corwin, Silvio Franz, and Francesco Zamponi, “Gardner physics in amorphous solids and beyond,” *The Journal of chemical physics* **151** (2019).
- [31] Huaping Li, Yuliang Jin, Ying Jiang, and Jeff ZY Chen, “Determining the nonequilibrium criticality of a gardner transition via a hybrid study of molecular simulations and machine learning,” *Proceedings of the National Academy of Sciences* **118**, e2017392118 (2021).
- [32] Pierfrancesco Urbani, Yuliang Jin, and Hajime Yoshino, “The gardner glass,” in *Spin Glass Theory and Far Beyond: Replica Symmetry Breaking After 40 Years* (World Scientific, 2023) pp. 219–238.
- [33] Patrick Charbonneau, Eric I Corwin, Giorgio Parisi, and Francesco Zamponi, “Jamming criticality revealed by removing localized buckling excitations,” *Physical review letters* **114**, 125504 (2015).
- [34] Yinqiao Wang, Jin Shang, Yuliang Jin, and Jie Zhang, “Experimental observations of marginal criticality in granular materials,” *Proceedings of the National Academy of Sciences* **119**, e2204879119 (2022).
- [35] Carl P Goodrich, Andrea J Liu, and Sidney R Nagel, “Finite-size scaling at the jamming transition,” *Physical review letters* **109**, 095704 (2012).
- [36] Peter Olsson and Stephen Teitel, “Critical scaling of shear viscosity at the jamming transition,” *Physical review letters* **99**, 178001 (2007).
- [37] Peter Olsson and S Teitel, “Critical scaling of shearing rheology at the jamming transition of soft-core frictionless disks,” *Physical Review E* **83**, 030302 (2011).
- [38] Takeshi Kawasaki, Daniele Coslovich, Atsushi Ikeda, and Ludovic Berthier, “Diverging viscosity and soft granular rheology in non-brownian suspensions,” *Physical Review E* **91**, 012203 (2015).
- [39] Claus Heussinger and Jean-Louis Barrat, “Jamming transition as probed by quasistatic shear flow,” *Physical review letters* **102**, 218303 (2009).
- [40] Daniel Vagberg, Daniel Valdez-Balderas, MA Moore, Peter Olsson, and Stephen Teitel, “Finite-size scaling at the jamming transition: Corrections to scaling and the correlation-length critical exponent,” *Physical Review E* **83**, 030303 (2011).
- [41] Thibault Bertrand, Robert P Behringer, Bulbul

- Chakraborty, Corey S O’Hern, and Mark D Shattuck, “Protocol dependence of the jamming transition,” *Physical Review E* **93**, 012901 (2016).
- [42] Marco Baity-Jesi, Carl P Goodrich, Andrea J Liu, Sidney R Nagel, and James P Sethna, “Emergent so (3) symmetry of the frictionless shear jamming transition,” *Journal of Statistical Physics* **167**, 735–748 (2017).
- [43] Yuliang Jin and Hajime Yoshino, “A jamming plane of sphere packings,” *Proceedings of the National Academy of Sciences* **118**, e2021794118 (2021).
- [44] Pinaki Chaudhuri, Ludovic Berthier, and Srikanth Sastry, “Jamming transitions in amorphous packings of frictionless spheres occur over a continuous range of volume fractions,” *Physical review letters* **104**, 165701 (2010).
- [45] Misaki Ozawa, Takeshi Kuroiwa, Atsushi Ikeda, and Kunimasa Miyazaki, “Jamming transition and inherent structures of hard spheres and disks,” *Physical review letters* **109**, 205701 (2012).
- [46] SS Ashwin, Jerzy Blawdziewicz, Corey S O’Hern, and Mark D Shattuck, “Calculations of the structure of basin volumes for mechanically stable packings,” *Physical Review E* **85**, 061307 (2012).
- [47] Stefano Martiniani, K Julian Schrenk, Kabir Ramola, Bulbul Chakraborty, and Daan Frenkel, “Numerical test of the edwards conjecture shows that all packings are equally probable at jamming,” *Nature physics* **13**, 848–851 (2017).
- [48] David J Pine, Jerry P Gollub, John F Brady, and Alexander M Leshansky, “Chaos and threshold for irreversibility in sheared suspensions,” *Nature* **438**, 997–1000 (2005).
- [49] Laurent Corte, Paul M Chaikin, Jerry P Gollub, and David J Pine, “Random organization in periodically driven systems,” *Nature Physics* **4**, 420–424 (2008).
- [50] Carl F Schreck, Robert S Hoy, Mark D Shattuck, and Corey S O’Hern, “Particle-scale reversibility in athermal particulate media below jamming,” *Physical Review E* **88**, 052205 (2013).
- [51] Kentaro Nagasawa, Kunimasa Miyazaki, and Takeshi Kawasaki, “Classification of the reversible–irreversible transitions in particle trajectories across the jamming transition point,” *Soft matter* **15**, 7557–7566 (2019).
- [52] Pallabi Das, HA Vinutha, and Srikanth Sastry, “Unified phase diagram of reversible–irreversible, jamming, and yielding transitions in cyclically sheared soft-sphere packings,” *Proceedings of the National Academy of Sciences* **117**, 10203–10209 (2020).
- [53] Corey S O’Hern, Stephen A Langer, Andrea J Liu, and Sidney R Nagel, “Random packings of frictionless particles,” *Physical Review Letters* **88**, 075507 (2002).
- [54] K Binder, “Finite size effects on phase transitions,” *Ferroelectrics* **73**, 43–67 (1987).
- [55] Dapeng Bi, Jie Zhang, Bulbul Chakraborty, and Robert P Behringer, “Jamming by shear,” *Nature* **480**, 355–358 (2011).
- [56] Nishant Kumar and Stefan Luding, “Memory of jamming–multiscale models for soft and granular matter,” *Granular Matter* **18**, 58 (2016).
- [57] Yiqiu Zhao, Jonathan Barés, Hu Zheng, Joshua ES Socolar, Robert P Behringer, *et al.*, “Shear-jammed, fragile, and steady states in homogeneously strained granular materials,” *Physical review letters* **123**, 158001 (2019).
- [58] Kurt Binder, “Theory of first-order phase transitions,” *Reports on progress in physics* **50**, 783 (1987).
- [59] Varghese Babu, Deng Pan, Yuliang Jin, Bulbul Chakraborty, and Srikanth Sastry, “Dilatancy, shear jamming, and a generalized jamming phase diagram of frictionless sphere packings,” *Soft Matter* **17**, 3121–3127 (2021).
- [60] Michael Gofman, Joan Adler, Amnon Aharony, A Brooks Harris, and Moshe Schwartz, “Evidence for two exponent scaling in the random field ising model,” *Physical review letters* **71**, 1569 (1993).
- [61] Thomas Nattermann, “Theory of the random field ising model,” in *Spin glasses and random fields* (World Scientific, 1998) pp. 277–298.
- [62] Misaki Ozawa, Ludovic Berthier, Giulio Biroli, Alberto Rosso, and Gilles Tarjus, “Random critical point separates brittle and ductile yielding transitions in amorphous materials,” *Proceedings of the National Academy of Sciences* **115**, 6656–6661 (2018).
- [63] Kaihua Zhang, Xinyang Li, Yuliang Jin, and Ying Jiang, “Machine learning glass caging order parameters with an artificial nested neural network,” *Soft Matter* **18**, 6270–6277 (2022).
- [64] Harukuni Ikeda, “Control parameter dependence of fluctuations near jamming,” *The Journal of Chemical Physics* **158** (2023).
- [65] Dapeng Bi, Silke Henkes, Karen E Daniels, and Bulbul Chakraborty, “The statistical physics of athermal materials,” *Annu. Rev. Condens. Matter Phys.* **6**, 63–83 (2015).
- [66] Giorgio Parisi, Yoav G Pollack, Itamar Procaccia, Corrado Rainone, and Murari Singh, “Robustness of mean field theory for hard sphere models,” *Physical Review E* **97**, 063003 (2018).
- [67] Erik Bitzek, Pekka Koskinen, Franz Gähler, Michael Moseler, and Peter Gumbsch, “Structural relaxation made simple,” *Physical review letters* **97**, 170201 (2006).

Extended Data

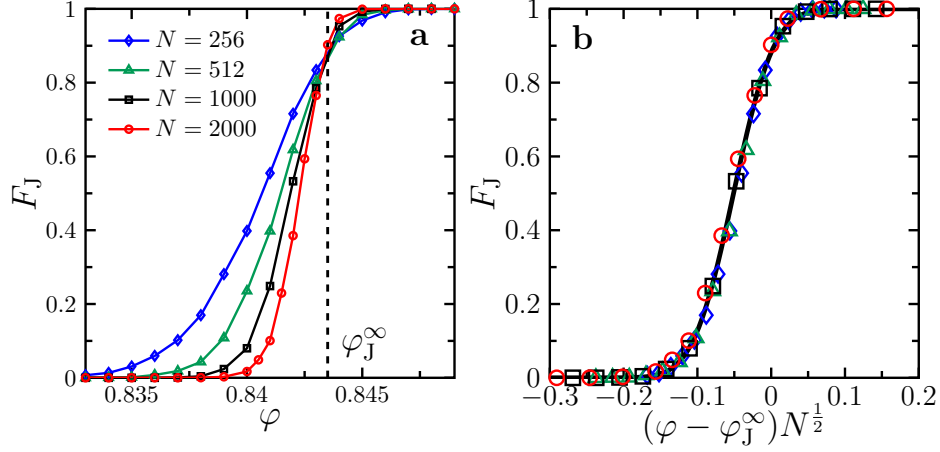


FIG. E1. **Distribution of the coordination number in two dimensions for $\gamma_{\max} = 1$.** (a) Fraction of jammed states F_J as a function of φ for a few different N . The intersection of curves gives $\varphi_J^\infty = 0.8435$. (b) The data points of F_J with different N collapse as a function of $(\varphi - \varphi_J^\infty)N^{1/2}$. The solid line represents the fitting according to Eq. (4), with two fitting parameters $u = 0.051$ and $\sigma_\varphi = 0.043$.

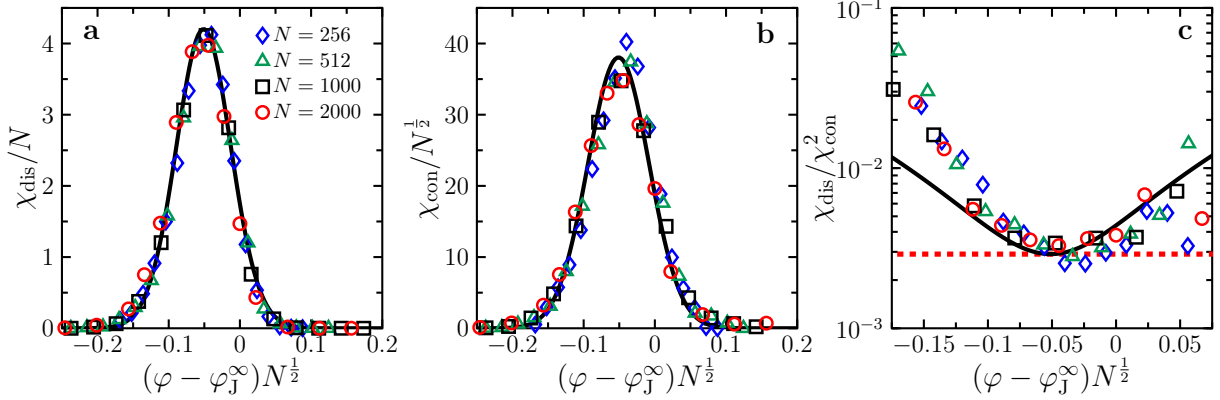


FIG. E2. **Susceptibilities in two dimensions for $\gamma_{\max} = 1$.** (a) The disconnected susceptibility χ_{dis} rescaled by N , (b) the connected susceptibility χ_{con} rescaled by $N^{1/2}$, and (c) the ratio between χ_{dis} and χ_{con}^2 are plotted as functions of $(\varphi - \varphi_J^\infty)N^{1/2}$. The solid black lines in (a-c) are Eqs. (5), (6) and (7) respectively. The dashed red line in (c) is the constant term in Eq. (7), i.e., $\chi_{\text{dis}}/\chi_{\text{con}}^2 = \pi\sigma_\varphi^2/2$. To draw these lines, we use $u = 0.051$ and $\sigma_\varphi = 0.043$ obtained from the fitting in Fig. E1b. Symbols in (a-c) have the same meanings as indicated in the legend of (a).

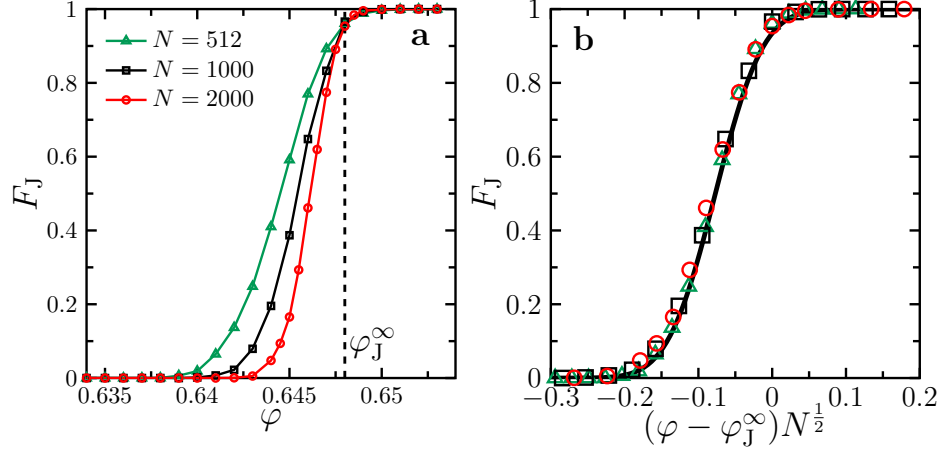


FIG. E3. **Distribution of the coordination number in three dimensions.** (a) Fraction of jammed states F_J as a function of φ for a few different N . The intersection of curves gives $\varphi_J^\infty = 0.648$. (b) The data points of F_J with different N collapse as a function of $(\varphi - \varphi_J^\infty)N^{1/2}$. The solid line represents the fitting according to Eq. (4), with two fitting parameters $u = 0.077$ and $\sigma_\varphi = 0.051$.

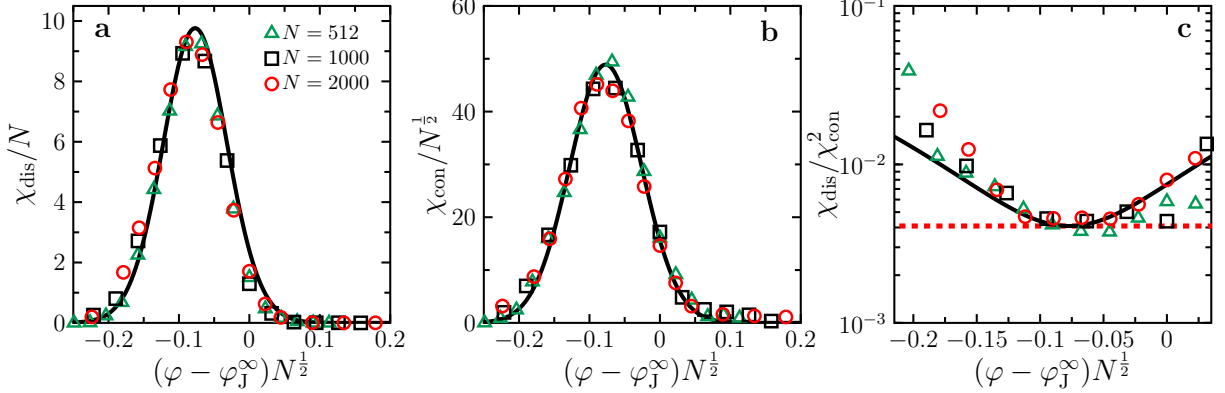


FIG. E4. **Susceptibilities in three dimensions.** (a) The disconnected susceptibility χ_{dis} rescaled by N , (b) the connected susceptibility χ_{con} rescaled by $N^{1/2}$, and (c) the ratio between χ_{dis} and χ_{con}^2 are plotted as functions of $(\varphi - \varphi_J^\infty)N^{1/2}$. The solid black lines in (a-c) are Eqs. (5), (6) and (7) respectively. The dashed red line in (c) is the constant term in Eq. (7), i.e., $\chi_{\text{dis}}/\chi_{\text{con}}^2 = \pi\sigma_\varphi^2/2$. To draw these lines, we use $u = 0.077$ and $\sigma_\varphi = 0.051$ obtained from the fitting in Fig. E3b. Symbols in (a-c) have the same meanings as indicated in the legend of (a).